ACS APPLIED ENERGY MATERIALS

www.acsaem.org Article

Selection of Polymer Segment Species Matters for Electrolyte Properties and Performance in Lithium Metal Batteries

Min-Huei Chiou, Elisabeth Verweyen, Diddo Diddens, Lennart Wichmann, Christina Schmidt, Kerstin Neuhaus, Aditya Choudhary, Dmitry Bedrov, Martin Winter, and Gunther Brunklaus*

Cite This: *ACS Appl. Energy Mater.* 2023, 6, 4422−4436 Read Online

ACCESS | Metrics & More | Article Recommendations | Supporting Information

ABSTRACT: Control of homogeneous lithium deposition governs prospects of advanced cell development and practical applications of high-energy-density lithium metal batteries. Polymer electrolytes are thus explored and employed to mitigate the growth of high-surface-area lithium species while enhancing the reversibility of the lithium reservoir upon cell cycling. Herein, an in-depth understanding of the distribution of membrane properties and lithium deposition behavior affected by the selection of polymer segment species is derived. It is demonstrated that severely localized lithium deposits featuring needle-like morphologies may be readily observed when electrostatic fields (or partial charges) and the amount of Li^+ coordinators of the primary and secondary polymer segment species appear rather dissimilar, leading to a sudden cell failure at early stages of cell operation. In comparison, employment of optimized copolymer electrolytes enables superior cell performance at 1C even with thicker cathodes (6.3 mg cm^{-2}). Additionally, the improvement of cell-cycling stability due to enhancement of similarity of dipole moments and partial charge distributions among copolymer segments are also demonstrated for different polymer systems, contributing to avoidance of undesired lithium protrusions, also reflecting a viable concept for the design of future copolymer electrolytes.

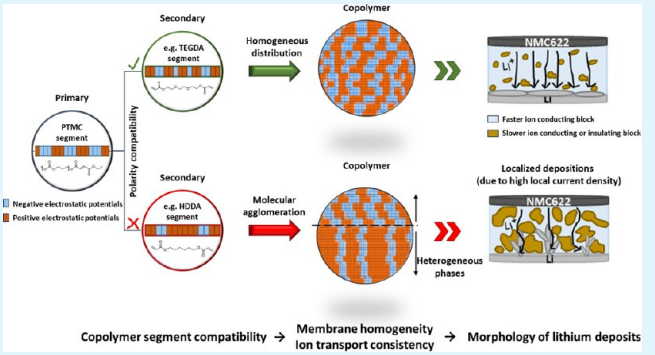

KEYWORDS: *membrane homogeneity, phase separation, consistency of ion transport, lithium deposition, polarity compatibility, copolymer, plasticizer distribution*

INTRODUCTION

On a mission to transform energy storage, next-generation solid-state lithium metal batteries (LMBs) affording high safety and enhanced energy density are expected to govern the vehicle market after the year 2030 (Battery2030+). In addition to integration of complex technology, a major challenge of such batteries constitutes reliable control and achievement of homogeneous lithium deposition. In this respect, polymers possessing prominent features, including, e.g., sufficient compressive mechanical properties, good affinity and contacts against the electrodes, and durable electrochemical stability toward lithium metal, are considered highly suitable electrolyte candidates that eventually mitigate the growth of high-surface-area lithium (HSAL) deposits.[1] However, some other factors that potentially trigger the inhomogeneous distribution of current density, ultimately leading to dendrite growth upon cycling, should also be taken into account, including but not limited to the lithium host materials, anode interphases, and bulk electrolytes. Several approaches for amelioration of cell performance have been demonstrated from the perspective of host materials and interphase properties, such as employment of three-dimensional (3D) skeleton structures as lithium hosts,[2] in this way regulating the distribution of current density near the lithium surfaces and exploitation of artificial solid electrolyte interphase (SEI) to stabilize and homogenize the interface between the electrode and electrolyte.[3,4] Also, the impacts of electrolyte concentration gradients and mechanical features toward resulting morphologies of lithium deposits were critically discussed based on the models of Chazalviel or Monroe and Newman, respectively, emphasizing that polymer electrolytes with a high Li^+ transference number (e.g., system of single-ion conducting polymers) and mechanical modulus (e.g., range of MPa) can effectively suppress formation of HSAL deposits.[5,6] However, the presence of (localized) electrolyte membrane inhomogeneity that eventually could adversely affect the behavior of lithium deposits upon cycling is

Received: March 2, 2023
Accepted: March 29, 2023
Published: April 6, 2023

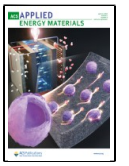

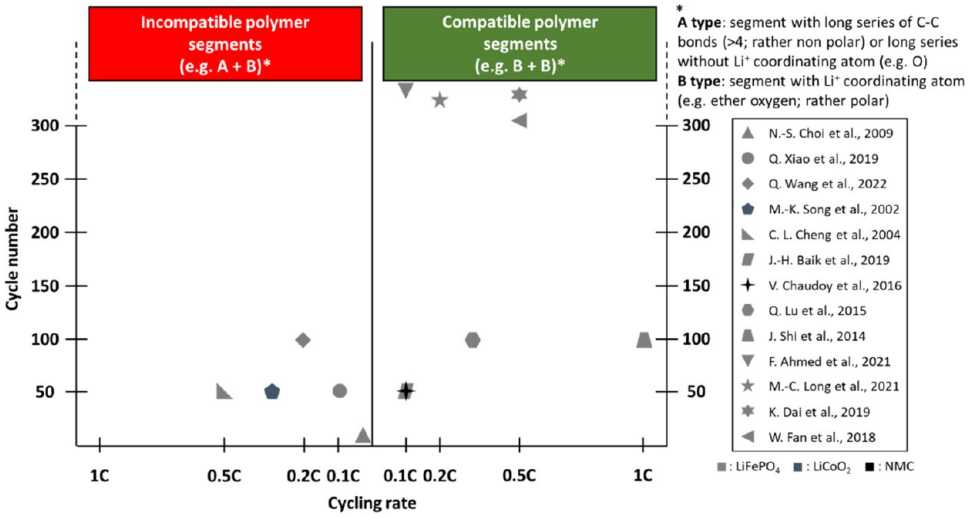

Figure 1. LMB cell performance (longevity) of gel polymer electrolytes containing at least two different polymer segments.[17−29]

often ignored and not systematically explored, especially not in the case of copolymer systems.

To boost salient features of common homopolymer electrolytes, additives, plasticizers, or other polymer species are often introduced, affording synergistic effects, such as a suitable balance of mechanical stability and ionic conductivity.[7,8] Note that different polymer architectures provide individual ion speciation based on lithium-ion coordination with functional groups and mobile components, thereby governing the overall ion transport capability within the materials (e.g., due to ion hopping, polymer segmental motion, or exchange among coordination shell constituents).[9] Nevertheless, general guidance for designing mixed electrolytes is still incomprehensive and in practice might lead to defects of electrolyte microstructures. For instance, in the case of block copolymer systems, at least two incompatible or partially compatible polymer segments composed of independent monomers are exploited to attain microphase separation, thereby offering defined functional domains; some of them enable the formation of continuous pathways dominating charge carrier transport (called the salt solvating polymer block established by polar groups such as −O−, C═O, −N−, −S−, or C═N),[9] and the others solely enhance the mechanical rigidity (mechanically robust but ion-insulating block).[10] Pronounced phase separation or uncontrollable agglomeration and orientation of these domains may trigger uneven electrodeposition of lithium metal and the occurrence of local defects, especially upon the exposure to a critical current density, which however tends to be neglected even though the differences of local ionic conductivity are obviously recognizable.[11−13] In a current study, it was elucidated that the behavior of heterogeneous lithium deposits is strongly associated with membrane phase separation in the case of polymer blend systems, and though the invoked concept appears applicable to other block copolymers or ceramic hybrid electrolytes, no insightful details of structural chemistry were discussed.[14]

Apart from polymer blends or block copolymers, a local disparity of charge carrier transport could also emerge in the system of "random" (cross-linked) copolymers (e.g., asymmetric copolymer)[15] when the chemical structures and entities of the introduced monomers/oligomers have disparate lithium-ion coordination sites or appear incompatible in view of polarity, thereby eventually giving rise to molecular aggregation and a rather nonuniform distribution of electrolyte properties.[16] This inconsistency of ion transport could detrimentally cause cell-cycling instabilities. Moreover, in plasticized (gel) polymer systems, a plasticizer is mainly used to boost overall conductivity, but the polarity divergences within the polymer membranes might additionally govern the resulting inhomogeneity of any plasticizer distribution that potentially triggers even more hazards based on the formation of severely agglomerated lithium deposits upon electrochemical cycling.[13] As indicated from Figure 1, LMB cell performances with the published gel polymer electrolytes that contain "incompatible" polymer segments are overall limited by slow cycling rates and short cycle numbers. Notably, recently reported electrolyte materials that afford promising cycling behaviors mostly have "compatible" copolymer network structures. But so far, no research has paid attention to this interrelation.

In the present work, the impacts of compatibility based on copolymer structural chemistries (e.g., electrostatic potentials) on membrane homogeneity and electrochemical cycling performance of cells are investigated. A multifunctional and carbonate-based oligomer [modified poly(trimethylene carbonate)-grafted cyclodextrins (PTMC-GCDs)] was introduced as the primary segment species due to its amorphous structure and promising electrochemical features (including a high transference number of ∼0.6 and a wide oxidative stability window of up to 5 V, as revealed by a previous work),[30] and several types of monomer species with distinct chemical bonds and polarities were explored as secondary segment species to establish various network structures in the presence of a plasticizer or mobilizer while systematically evaluating the corresponding electrolyte properties and electrochemical features in NMC622||Li- and Cu||Li-type cells. Notably, behaviors of molecular aggregations and lithium-ion coordination can be clearly elucidated by atomic force microscopy (AFM) images and molecular dynamics (MD) simulations. In combination with scanning electron microscopy (SEM) images and solid-state NMR data, the results indicate that the deposited lithium morphology is strongly associated with the polymer membrane homogeneity, as mainly determined by the actual structural compatibility between both the primary and secondary segment species. Namely, very dissimilar molecular electrostatic fields (or partial charges) among the considered

https://doi.org/10.1021/acsaem.3c00571
ACS Appl. Energy Mater. 2023, 6, 4422−4436

Scheme 1. Electrolyte Constituents and Structures of Multifunctional Oligomers (Primary Species) and Different Configurations of the Considered Monomers (Secondary Species)

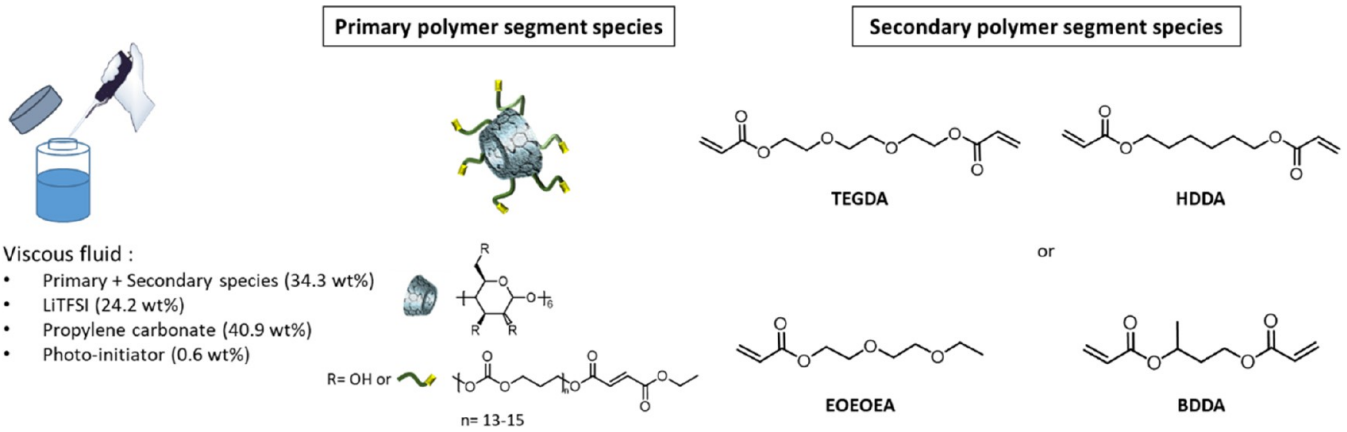

electrolyte constituent species likely result in severely localized lithium deposition and unanticipated cell failures upon electrochemical operation. The same behaviors can also be observed in the poly(ethylene oxide) (PEO)-based system. Thus, parameters for the rational design of electrolytes in plasticized (cross-linked) copolymer systems are reconsidered, including the enhancement of membrane homogeneity and the consistency of achievable charge carrier transport, which can be further elevated by increasing the similarity of molecular electrostatic fields among the utilized polymer species.

EXPERIMENTAL SECTION

Materials. The multifunctional carbonate-based oligomers (modified PTMC-grafted α-cyclodextrins; M_n ~11k) with 90% modification at the terminal groups (hydroxyl group to acrylate) were prepared according to a reported procedure (please see ^{1}H NMR and gel permeation chromatography (GPC) data collected in Figure S1, Supporting Information).[30] 1,6-Hexanediol diacrylate (HDDA, 99%, dried over 4 Å molecular sieves) and triethylene glycol diacrylate (TEGDA, 90%, dried over 4 Å molecular sieves) were received from abcr GmbH. 2,2-Dimethoxy-2-phenylacetophenone (DMPA, 99%), poly(ethylene glycol)diacrylate (PEGDA; M_n 700), 2-(2-ethoxyethoxy)ethyl acrylate (EOEOEA, dried over 4 Å molecular sieves), and 1,3-butanediol diacrylate (BDDA, >98%, dried over 4 Å molecular sieves) were purchased from Sigma Aldrich, Germany. Propylene carbonate (PC) and lithium bis-trifluoro-methane-sulfonimide (LiTFSI) were obtained from BASF and Solvionic, respectively. $LiNi_{0.6}Mn_{0.2}Co_{0.2}O_2$ (NMC622) cathode sheets (with a mass loading of 2.5 mg cm^{-2} and a layer thickness of 17 μm) were prepared following established protocols,[30] and a thicker NMC622 cathode sheet (6.3 mg cm^{-2}) was purchased from CUSTOMCELLS.

Preparation of the Quasi-Solid Copolymer Electrolyte. According to a previous work,[30] a high fraction of secondary species would lead to a lower capacity retention of cells operated with these carbonate-based polymer electrolytes. Thus, the mass ratio between primary (modified PTMC-GCDs) and secondary species was set to 3:1. PC was selected as an optimized plasticizer in this PTMC-based electrolyte system due to its superior cycling performance compared to other carbonate-based solvents, such as dimethyl carbonate (DMC) and ethylene carbonate/propylene carbonate (EC/PC) with or without fluoroethylene carbonate (FEC) additives, which has also been demonstrated in our previous work. A viscous fluid comprising a 25.7 wt % carbonate-based multifunctional oligomer (primary segment species), an 8.6 wt % monomer (secondary segment species), as well as 24.2 wt % LiTFSI, 40.9 wt % PC, and 0.6 wt % DMPA was cast between two mylar foils with a gap of 130 μm after blending. The mixture was photocured for 90 min in an UVACUBE 100 to ensure complete cross-linking (absence of C=C bonds).[30] In total, five quasi-solid and cross-linked electrolyte samples were explored, containing the PTMC homopolymer (1), TEGDA (2), EOEOEA (3), HDDA (4), and BDDA (5) copolymers (see in Scheme 1 and network formation in Scheme S1, Supporting Information).

PEO-based plasticized electrolytes were prepared in the same way but replacing modified PTMC-GCDs by PEGDA (M_n 700) as the primary segment species.

Material Characterization. *Electrostatic Potential.* To quantify the polarity of the individual polymer and plasticizer species, density functional theory (DFT) calculations were carried out with the program Gaussian 16.[31] All calculations were performed at the B3LYP/def2-TZVP level of theory, including the implicit SMD solvation model with built-in parameters for acetone,[32] which has a similar dielectric constant as typical liquid carbonate electrolytes.[33−35] For all optimized geometries, the electron density and electrostatic potentials were computed. More details including the computation of partial charge are given in Figure S2 and Table S1 (Supporting Information).

Rheology. A modular compact rheometer (MCR102) from Anton Paar equipped with a measuring system of PP15-SN71066 (diameter of 15 mm) was utilized to determine the mechanical properties of the polymer membranes. The amplitude (γ) was fixed at a constant value of 0.5%, and the angular frequency was varied in the range of 200−1 rad s^{-1} while 1N of normal force was applied.

Scanning Electron Microscopy. SEM analysis was used to assist in the inspection of lithium surface morphologies and lithium deposits in the presence of polymer membranes and the Cu substrate. Multiple areas of each sample were analyzed at an Auriga CrossBeam workstation from Carl Zeiss (Germany), exploiting an acceleration voltage of 3 kV.

Atomic Force Microscopy (AFM). All AFM measurements were performed using a Cypher-ES AFM (Asylum Research by Oxford Instruments, U.K.) with PPP-NCSTPt probes (Nanosensors, Switzerland). The probes show a nominal force constant in the range of 7.4 N m^{-1} and are coated with a Pt/Ir alloy to ensure conductivity for Kelvin probe force microscopy (KPFM) measurements. All of the samples were stored and examined in air. For topography measurements, the phase shifts of the mechanical excitation of the cantilever and local surface potential were done simultaneously in a two-pass experiment in intermittent contact. The mode that enables surface potential measurements is referred to as Kelvin probe force microscopy.[36] For this, the AFM tip is scanned above the surface in a defined height of 30 nm, and the contact potential difference between the metal-coated tip and the sample is recorded, which is equivalent to a local surface potential of the considered samples. For image analysis, the program MountainsSPIP Starter 8.0 (Digital Surf, France) was employed.

Molecular Dynamics (MD) Simulations. Atomistic MD simulations were conducted using Atomistic Polarizable Potential for

https://doi.org/10.1021/acsaem.3c00571
ACS Appl. Energy Mater. 2023, 6, 4422−4436

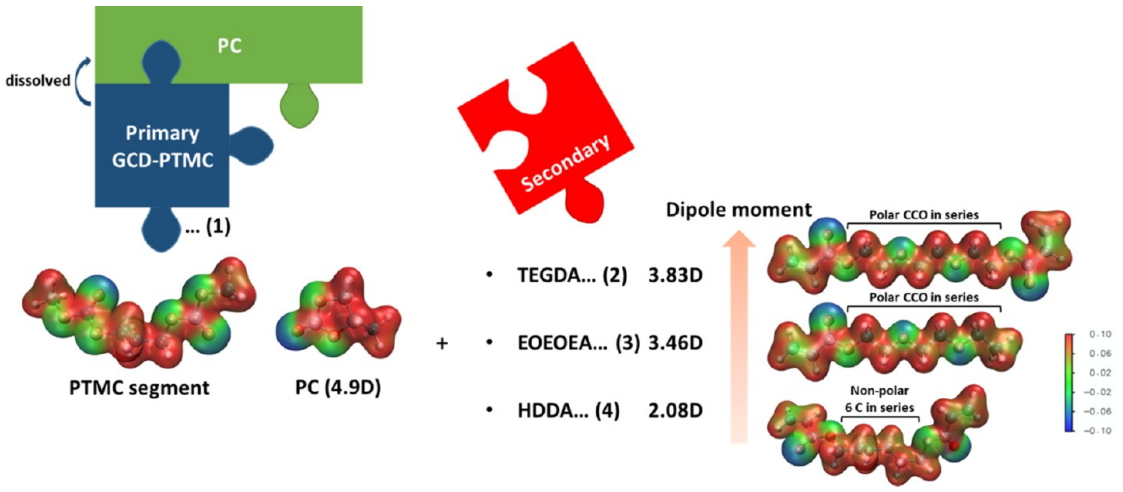

Figure 2. Components of the introduced electrolytes (1)−(4), containing the plasticized and cross-linked homopolymer (1), the TEGDA copolymer (2), the EOEOEA copolymer (3), and the HDDA copolymer (4), respectively. Calculated electrostatic potentials around atoms of the PTMC segment, propylene carbonate, and the considered secondary oligomer species (in their extended conformation) as obtained from DFT calculations.

Liquids, Electrolytes & Polymers (APPLE&P) using an in-house-developed simulation package.[37,38] This polarizable force field has been extensively used to investigate polymer electrolytes.[39−41] In this force field, each force center has an isotropic polarizability, and the induced point dipoles are computed using the self-consistent approach. We used the Thole screening factor of 0.2 to prevent "polarization catastrophe".[42] All of the bonds were constrained using the SHAKE algorithm.[43] The cutoff distance of 15.0 Å was used to calculate the van der Waals and the real part of electrostatic interactions. The Ewald summation method was utilized to compute the reciprocal part of electrostatic interactions. During the simulation, temperature and pressure were controlled using a Nosé−Hoover thermostat with a frequency of 0.01 fs^{-1} and an Anderson−Hoover barostat with a frequency of 0.0005 fs^{-1}.[44,45] A multiple-time integration scheme was incorporated to enhance the computational efficiency.[46] A small time step of 0.5 fs was used for calculating bonds and bends; a medium time step of 1.5 fs was used for calculating torsions and short-range (<8.0 Å) nonbonded interactions; and a large time step of 3.0 fs was used for calculating the long-range nonbonded interactions (>8.0 Å) and the reciprocal part of the Ewald summation.

Two sets of systems were investigated. In the first set, the additives (namely, secondary segment species) were not part of the polymer and were dissolved in the solvent, while in the second set, the additive ends were assumed to react with the polymer, forming a comb-branched chain with the side chains being a mixture of PTMC and the corresponding additive. The objectives of simulating two sets are to understand the behavior of additives before the polymerization begins and after the completion of polymerization. In both cases, the molar ratio of PTMC:TEGDA:Li^+:TFSI:PC is 6:14:34:34:162 and PTMC:HDDA:Li^+:TFSI:PC is 6:15:34:34:162. In initial configurations, all molecules were randomly placed in a large cubic simulation box of size 300 Å. The dimension of the box was shrunk over 3 ps to achieve a density of about 1 g/cm^3. The obtained system was run in the NVT ensemble at a high temperature (500 K) for 3 ns to allow relaxation of polymer degrees of freedom. Then, the systems were cooled down to 300 K, followed by an equilibration run in the NPT ensemble for 3 ns. Production runs were over 10 ns in the NPT ensemble. Additional details including comparability of linear and grafted CD systems are given in Table S2 and Figure S3 (Supporting Information).

^{7}Li Solid-State Nuclear Magnetic Resonance. Coin cells (diameter of 10 mm) of Cu||Li (1M HCl-treated Cu) as well as NMC622||Li were analyzed with respect to deposited lithium morphologies after electrochemical cell operation. Static ^{7}Li NMR experiments were performed at room temperature employing an AVANCE III 200 MHz spectrometer operating at a magnetic field of 4.7 T with a ^{7}Li Larmor frequency of 77.9 MHz. All of the NMR spectra were recorded with a saturation recovery sequence at a pulse length of 15 μs and a relaxation delay of 0.5 s, averaging 2048 scans for each spectrum. The ^{7}Li NMR spectra were referenced with respect to 1M LiCl solution (^{7}Li, 0 ppm). Data analysis was done with BRUKER Topspin 3.5 software applying automatic phase correction. The total signal intensity of the peaks reflecting Li metal species was integrated over the chemical shift range from 180 to 330 ppm and fitted considering three distinct lithium metal species.[47]

Electrochemical Characterization. *Lithium-Ion Conductivity.* The fractional conductivity of lithium ions was derived from the overall ionic conductivity multiplied with the Li^+ transference number. Electrochemical impedance spectroscopy (EIS) was conducted to derive overall ionic conductivities using an Autolab device. Polymer membranes were punched to 12 mm-diameter disks (thickness of 100−150 μm) and assembled in coin cells (CR2032) between two polished stainless-steel electrodes. Here, temperature ranges of 0−70 °C with 10 °C increment per step scanning over a frequency range from 1 Hz to 1 MHz with a 10 mV sinus amplitude after a preheating step (20−70 °C) were applied. The transference numbers were examined in Li||Li cells at 20, 40, and 60 °C, after a duration of one-day equilibration of all of the samples at the moderate temperature of 40 °C. A DC polarization voltage (ΔV) of 10 mV was applied for potentiostatic polarization; the resulting current was recorded over time, and corresponding impedance spectra were collected between 1 Hz and 1 MHz before and after polarization. For data analysis, assuming negligible ion−ion interactions, an approach proposed by Watanabe et al. was exploited since the interfacial resistance does not notably vary after cell polarization.[48]

Cell Assembly and Cycling Conditions. NMC622||Li cells were built in a two-electrode coin-cell configuration in a dry room (dew point below −66 °C). The diameters of the anode, cathode, and polymer electrolytes were set to 14, 10, and 12 mm, while the layer thicknesses were 300 μm, 37 μm (including 20 μm of Al foil; mass loading of 2.5 mg cm^{-2}), and 100−130 μm, respectively. A Mylar-foil ring (outer diameter: 16 mm; inner diameter: 13 mm) was placed at the outer area of the polymer electrolyte to cover residual lithium metal to avoid short circuit. In addition, Cu||Li (1M HCl-treated Cu) were also assembled, following the same sandwich method as described above. All of the cells were cycled on a Maccor 4000 battery analysis system at 20 and 60 °C, respectively, and NMC622||Li were operated at a voltage range of 4.3 and 3 V (constant current, theoretical specific capacity of 180 mAh g^{-1}).

https://doi.org/10.1021/acsaem.3c00571
ACS Appl. Energy Mater. 2023, 6, 4422−4436

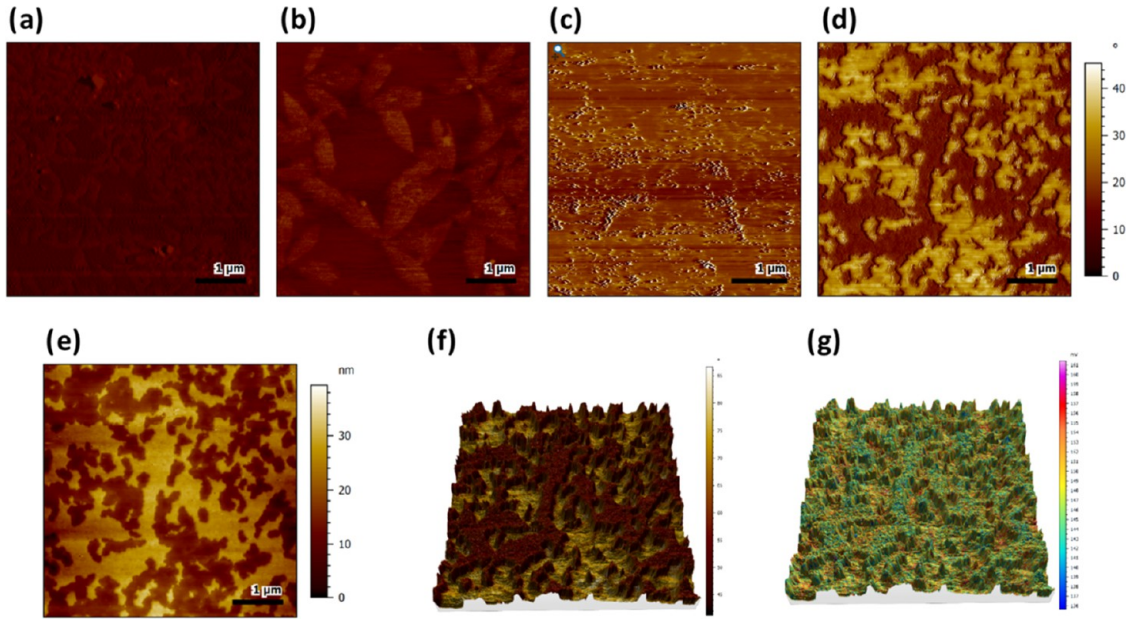

Figure 3. (a–d) AFM phase images of electrolytes (1)–(4), respectively; small artifacts (stripes) exist in (c) caused by stuck cantilever at the polymer membrane due to the surface stickiness. (e) Topography image of electrolyte (4). (f) Three-dimensional overlapped image of topography and phase shift and (g) 3D overlapped image of topography and surface potential.

RESULTS AND DISCUSSION

Impact of Selection of Secondary Polymer Species on Membrane Homogeneity. To consider the influence of structural and polar differences between primary and secondary polymer species as well as the resulting inhomogeneous electrolyte properties within formed membranes and limited electrochemical cell performance of "quasi-solid" copolymer electrolytes, we investigated PTMC-based polymer electrolytes. Herein, multifunctional PTMC-GCDs comprise the primary polymer species, while several monomers with different chemical bonds are individually introduced as secondary polymer species, involving TEGDA, EOEOEA, and HDDA (as shown in Figure 2). Notably, electrolytes (2)–(4) are composed of primary and different secondary species that establish distinct copolymer networks in the presence of LiTFSI and PC, while electrolyte (1) is a plasticized and cross-linked PTMC homopolymer. DFT calculations reveal that a series of C–C bonds (six neighboring carbons in a row) in HDDA appears rather nonpolar compared to segments of TEGDA and EOEOEA containing few ether oxygens (C–C–O), thereby offering different degrees of compatibility with PTMC-GCDs, as determined by the similarity of electrostatic fields (or partial charges) among polymer segments.[19] Overall, electrolyte components of PTMC-GCDs, PC, and secondary species involving C–C–O bonds (e.g., TEGDA and EOEOEA) occur as relatively polar species that have larger differences of electron densities/partial charges among neighboring atoms (see Figure 2; data of patrial charge shown in Figure S2 and Table S1, Supporting Information). Hence, the selection among these various mono-/bifunctional monomers used as secondary polymer species could in principle impact compatibility between copolymer segments and lead to structural heterogeneities in the membrane and affect LMB cell performance.

To monitor membrane homogeneity, AFM constitutes a powerful tool that provides information on polymer membrane topography, including surface roughness and potential, elasticity/adhesion, and so on.[49,50] In Figure 3a–d, the comparison between phase images of each electrolyte clearly illustrates that the membrane of electrolyte (4) has rather strong color contrasts established by mechanically harder areas (small phase shift, darker) and comparatively softer domains (high phase shift, lighter), thus unambiguously highlighting inconsistent mechanical elasticity or adhesion present within the polymer membrane. This kind of extreme phase change is, however, absent in the other electrolyte materials. Besides, although topography images reveal that all membrane surfaces are generally flat (see Figure 3e, cases of electrolytes (2) and (3) shown in Figure S4a,b, Supporting Information), sharply defined elevated spots (light brown) can be readily observed in the case of electrolyte (4), exhibiting differences at the *z*-axial scale on the order of 20 nm. The 3D overlapped AFM image also discloses a good match between those domains in topography and phase shift, showing that the soft domains are only located at the surface depressions (see Figure 3f). This domain pattern presumably results from two incompatible segments of PTMC and HDDA that foster molecular agglomeration during blending or cross-linking/polymerizing the electrolyte precursors (solubility of PTMC-GCDs in various secondary segment species is shown in Figure S5, Supporting Information), even though the final DSC analysis in Figure S6 (Supporting Information) reflects only one glass-transition temperature.[51,52] In addition, the image of surface potential displays that the charges seem to be well distributed (Figure 3g), yet the areas possessing a higher surface potential (red color) mostly show up at the surface depressions (soft domain), whereas lower potential areas represent harder domains, also reflecting changes of the local electrolyte composition.

To better understand the underlying molecular-scale interactions and correlations that can lead to observed heterogeneity in the membrane, atomistic MD simulations were conducted for several related systems. The first set of systems comprised linear PTMC, representing primary

https://doi.org/10.1021/acsaem.3c00571
ACS Appl. Energy Mater. 2023, 6, 4422–4436

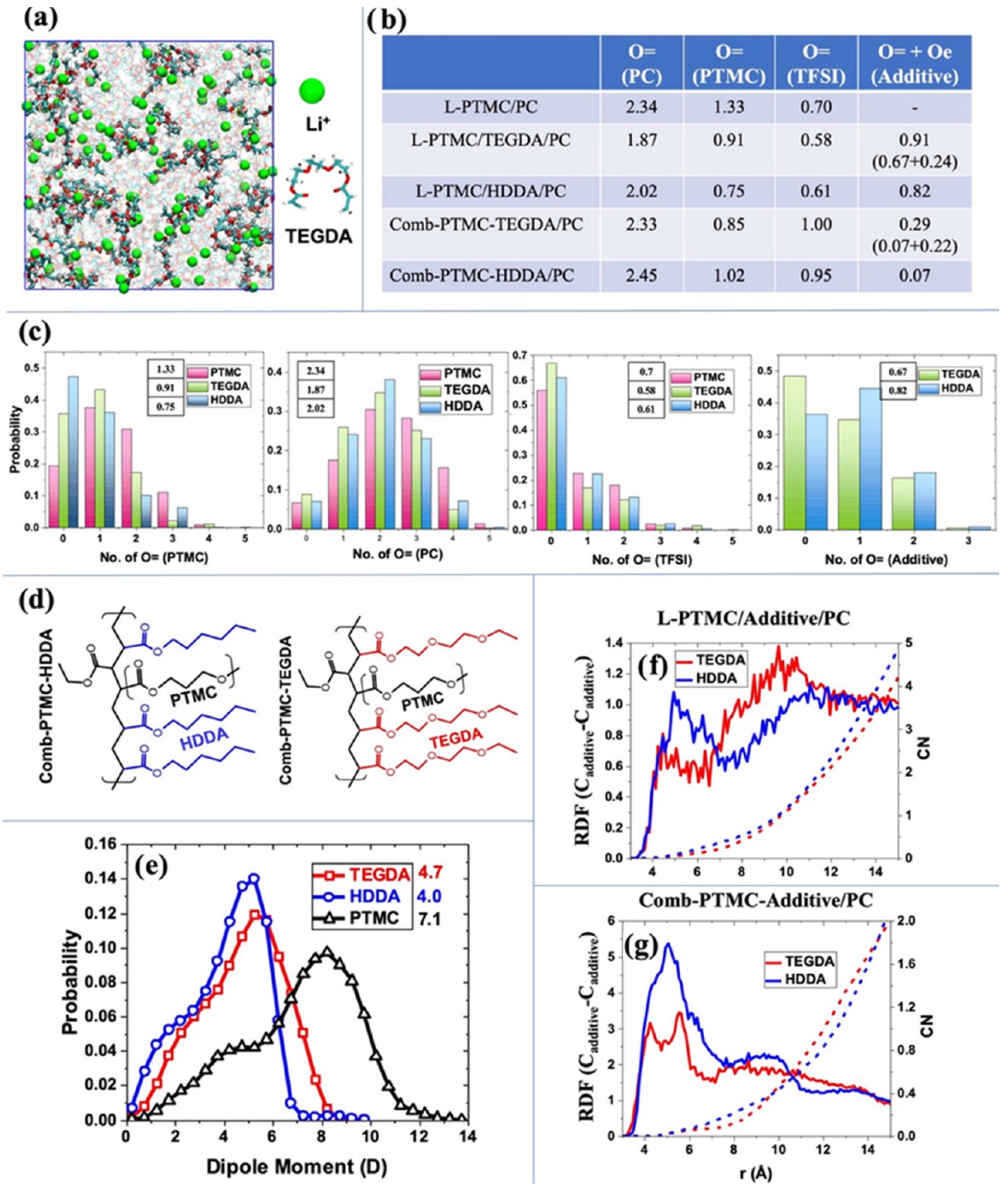

	O= (PC)	O= (PTMC)	O= (TFSI)	O= + Oe (Additive)
L-PTMC/PC	2.34	1.33	0.70	-
L-PTMC/TEGDA/PC	1.87	0.91	0.58	0.91 (0.67+0.24)
L-PTMC/HDDA/PC	2.02	0.75	0.61	0.82
Comb-PTMC-TEGDA/PC	2.33	0.85	1.00	0.29 (0.07+0.22)
Comb-PTMC-HDDA/PC	2.45	1.02	0.95	0.07

Figure 4. Results from MD simulations. (a) Snapshot of the L-PTMC/TEGDA/PC/LiTFSI system with Li^+ and TEGDA molecules highlighted; (b) average number of O atoms in the Li^+ first coordination shell; (c) probability distribution of funding a certain number of O atoms of different types in Li^+ coordination in L-PTMC/Additive/PC electrolytes (notation: PTMC, L-PTMC/PC electrolyte; TEGDA, L-PTMC/TEGDA/PC; HDDA, L-PTMC/HDDA/PC); (d) schematic illustration of comb-branched polymers representing the polymerized membrane; (e) distribution of instantaneous molecular dipole moments of components obtained from MD simulation trajectories (PTMC considers a dipole moment of two consecutive monomers in the chain); and (f) and (g) carbon−carbon radial distribution function of HDDA or TEGDA in L-PTMC/Additive/PC and Comb-PTMC-Additive/PC systems.

polymer species, and the corresponding additives used as the secondary segment species (HDDA or TEGDA), PC solvent, and Li-salt with compositions corresponding to experimental ratios. We refer to these systems as L-PTMC/Additive/PC. These systems represent the molecular interactions in the initial stages of membrane formation before polymerization reactions progress, and the systems can be considered as solutions. Figure 4a shows a snapshot of one of such systems highlighting the distribution of an additive (TEGDA) and Li^+ ions. As shown in Figure 2, each component in the system contains O atoms with negative partial charges. Double-bonded O atoms in PC, PTMC, TFSI, and end-groups of additives as well as the ether oxygens (e.g., in TEGDA) are the primary sources of atoms with negative partial charges that will preferentially interact with Li^+ and form its coordination shell. Analysis of radial distribution functions (RDFs) allows one to characterize the composition of the Li^+ first coordination shell (defined as 3.0 Å from the Li^+ center). On average, each Li^+

https://doi.org/10.1021/acsaem.3c00571
ACS Appl. Energy Mater. 2023, 6, 4422−4436

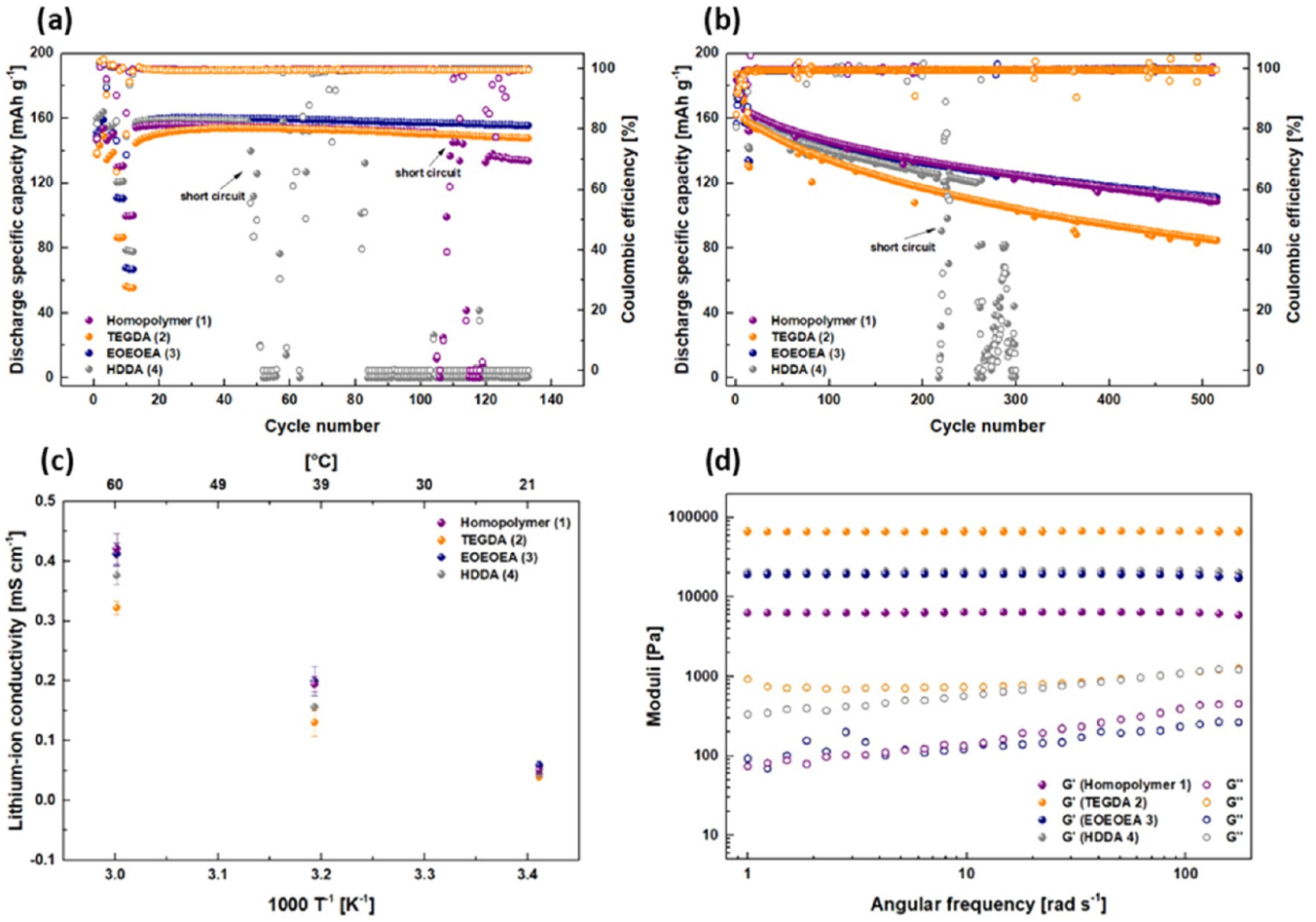

Figure 5. Cycling performance of NMC622||Li cells at (a) 20 °C and (b) 60 °C with electrolytes (1)−(4). Formation steps including 0.1/0.2/0.5/1C (3 cycles for each rate) were applied, and the long-term cycling proceeded at 0.2C for 120 cycles at 20 °C; formation steps of 0.1/0.2/0.5/1/2C and long-term cycling at 1C (~0.4 mA cm^{-2}) were executed at 60 °C. (c) Lithium-ion conductivity. (d) Storage G' and loss moduli G'' at 20 °C.

contains about 4.3−4.5 O atoms in the first coordination shell. However, as illustrated in Figure 4b,c, all species contribute to Li^+ coordination as the initial solution is mixed. The table in Figure 4b illustrates the average number of each oxygen type contributing to Li^+ coordination, while panels in Figure 4c provide probability distributions of finding a specific number of oxygens of a given type in the coordination shell. The double-bonded O atoms from the PC solvent contribute almost half of the coordination shell, while PTMC, TFSI, HDDA, or TEGDA has comparable contributions. In the system without any additives, PTMC has about 1.3 O atoms in the Li^+ coordination, while TFSI contributes only 0.7 oxygens, which is consistent with the high degree of dissociation of LiTFSI salt in these electrolytes. As HDDA or TEGDA is added to the system, their end-group double-bonded oxygens can compete for coordination with Li^+ and replace some fraction of PC and PTMC oxygens. For example, in the L-PTMC/HDDA/PC system, the coordination by PTMC and PC reduces from 1.3 to 0.75 and from 2.3 to 2.0, respectively, allowing about 0.8 O of HDDA in the Li^+ coordination. The relatively high negative charge of the double-bonded O entities and their steric exposure in the end-groups of HDDA and TEGDA make these entities efficient contributors to cation coordination.

As the polymerization reaction takes place and the double bonds of additives and PTMC end-groups react, the local environment near the double-bonded O atoms changes and becomes more sterically crowded. To mimic this effect, we have simulated systems containing comb-branched chains as illustrated in Figure 4d, in which the end-groups of additives and PTMC were assumed to undergo the polymerization reaction involving C═C bonds (systems referred to as Comb-PTMC-Additive/PC). As a result, the negatively charged oxygen atoms in the oligomer end-groups now have notably more steric interference from the backbone and neighboring groups. Simulations of Comb-PTMC-HDDA/PC and Comb-PTMC-TEGDA/PC systems with the same salt concentration reveal that once HDDA or TEGDA additives become part of the network, their ability to coordinate Li^+ drops substantially. Figure 4b shows that the average number of double-bonded O atoms of HDDA and TEGDA coordinating Li^+ drops by an order of magnitude (compared to free additive systems) and becomes less than 0.1. The coordination of Li^+ with ether O of TEGDA remains similar as in the system with free additives, hence still allowing TEGDA segments to participate in cation coordination.

The observed change in Li^+ coordination between the initial solution and the expected resulting polymeric structures comprising the membrane further emphasizes the complexity of membrane design and fabrication. Favorable interaction of Li-salt with some components and less favorable interaction with others can create additional thermodynamic forces to

https://doi.org/10.1021/acsaem.3c00571
ACS Appl. Energy Mater. 2023, 6, 4422−4436

drive structural heterogeneities. To further assess the compatibility of considered components, we have calculated the distribution of the dipole moments of HDDA and TEGDA additives, as well as the PTMC segment of similar length (two repeat units). The dipole moments shown in Figure 2 were calculated for a single, extended state conformation. However, these molecules/segments are conformationally flexible, and therefore, we used configurations from MD simulations to calculate the distributions of instantaneous dipole moments and the corresponding averages. Figure 4e illustrates that all key components show a broad range of dipole moments, with TEGDA averaging 4.7D, which is very close to the PC dipole moment of 4.9D,[19] while the HDDA molecule has about 20% lower dipole moment (around 4.0D). The effectively lower dipole moment of HDDA combined with the above-discussed inability to contribute to the Li^+ coordination after polymerization will likely make the HDDA segments thermodynamically less compatible with the other components (PTMC and PC), hence creating driving forces for HDDA segregation. Though TEGDA segments also lose the ability to contribute the double-bonded O atoms to Li^+ coordination after polymerization, their intrinsic higher dipole moment and the presence of ether O atoms still contributing to cation coordination make them more compatible in these electrolytes. To support this argument, we have analyzed the $C_{additive} - C_{additive}$ radial distribution function (RDF) in the L-PTMC/Additive/PC and Comb-PTMC-Additive/PC systems (Figure 4f,g). In electrolytes with free additives (i.e., before polymerization), the HDDA and TEGDA molecules have similar distributions, not showing any noticeable aggregation (the RDF is around 1.0, indicating a homogeneous spatial distribution). However, in the Comb-PTMC-Additive/PC systems, a noticeably larger aggregation of HDDA segments is observed compared to TEGDA segments. These trends are consistent with the AFM-observed heterogeneities discussed above.

Cycling Performance and Electrochemical and Physical Features of Electrolytes. In the light of achieving high-energy-density LMB cells, the NMC622 cathode that offers a higher capacity is employed for the evaluation of cell performance in this work.[53] In Figure 5a, the cycling result displays that electrolytes (1) and (4) in principal deliver higher discharge capacities (100 and 80 mAh g^{-1}) at rapid charge/discharge (1C) compared to electrolytes (2) and (3), thereby likely reflecting interphase formation with smaller Ohmic resistances for the underlying charge transfer as shown in Figure S7a,c (Supporting Information), especially considering that all electrolytes exhibit similar lithium-ion conductivities at 20 °C ($\sigma_{Li+} \sim 0.04$ mS cm^{-1} shown in Figure 5c). However, cells operated with both electrolytes encounter unanticipated short circuits, in particular in the case of electrolyte (4), where cell failures readily occur within 50 cycles, whereas cells cycling with the other electrolytes remain rather stable over hundred cycles. Note that upon increased operational temperature, the lithium-ion transport is boosted (displayed in Figure 5c); nevertheless, the increment of Li^+ conductivity of electrolyte (2) is relatively less pronounced, attributed to the higher cross-linking density and the presence of ether oxygens exhibiting a higher donor number, thereby affording somewhat stronger coordination to lithium ions, which eventually hinders the lithium-ion diffusion, in this way yielding smaller t_+ values (e.g., t_+ of 0.51, 0.32, 0.34, and 0.40 ±0.02 at 60 °C in the cases of electrolytes (1)−(4), respectively).[54] In theory, the electrochemical cell performance may be improved when exploiting the considered electrolytes at elevated temperatures owing to enhanced ionic conductivities and decreased resistances at the interfaces (see Figure S7b,c; Supporting Information);[55] however, a sudden termination of cycling still occurs (in the 205th cycle; Figure 5b) in the case of electrolyte (4) during long-term rapid cycling at 60 °C. Prior to short circuits emerging at both temperature conditions, strong capacity fading is not really observed, thus implying the absence of noteworthy electrolyte decompositions upon cycling.[56,57] Also, a suitable oxidative stability window of ∼4.4 V is identified (in Figure S8, Supporting Information), highlighting that the stability of the electrolytes against the NMC622 cathode active material is not the major cause that leads to this consequence. Overall, it is possible to attribute the cell failures to consequences of either limited mechanical resistance against electrolyte membrane deformation or localized inhomogeneity of electrolyte constituents within the polymer (as aforementioned) and thus uneven distribution of electrochemical properties that eventually contributes to heterogeneous lithium deposition upon cycling.[58−60]

On account of compressive mechanical properties that could facilitate HSAL suppression,[59] corresponding rheology measurements were performed to obtain shear moduli representing the degrees of mechanical resistance to deformation of the polymers. As displayed in Figure 5d, electrolyte (2) reveals superior mechanical strength (67 kPa) compared to electrolyte (4) (21 kPa) despite possessing similar degrees of cross-linking (as actively controlled by the present number of acryloyl groups). Since the bond energy of C−O (≈92 kcal mol^{-1}) is higher than that of C−C bonds (≈82 kcal mol^{-1}),[61] the actual energy to damage the corresponding polymer membrane is likely also higher, thereby implying that electrolyte (2) offers more reinforced structures against deformation. Electrolyte (4) presents weaker mechanical stability (lesser modulus) and substantially recognizable incompatibility of chemical structures between primary and secondary segment species (polar and nonpolar), rendering an unambiguous assignment of the origin of cell failures difficult.[59] Note that the observable reinforcement or weakening of the polymer materials' mechanical strength is correlated with the cross-linking density.[62−64] Electrolyte (3) is primarily employed for comparison to elucidate likely origins of cell failure when operating electrolyte (4), attributed to the presence of monofunctional EOEOEA instead of bifunctional TEGDA, in this way purposely reducing the degree of cross-linking and mechanical strength (19 kPa) of the resulting membrane.[65,66] Consequently, compared to electrolytes (1) and (3), sudden cell failure due to deficient mechanical properties can be excluded for electrolyte (4), since it actually has better mechanical stability. The unanticipated failure of cells operated with electrolyte (1) at 20 °C after a hundred cycles (Figure 5a) may be attributed to insufficient mechanical properties rather than membrane inhomogeneity of homopolymers.[67] The obtained cycling results are in good agreement with the data of corresponding AFM images and MD simulations (Figures 3 and 4) and support the notion that incompatibility between polymer segment species determines the actual distribution of membrane properties that eventually yields locally disparate lithium-ion transport rates that in turn might promote agglomerated lithium deposits and protrusions upon electrochemical cycling.

https://doi.org/10.1021/acsaem.3c00571
ACS Appl. Energy Mater. 2023, 6, 4422−4436

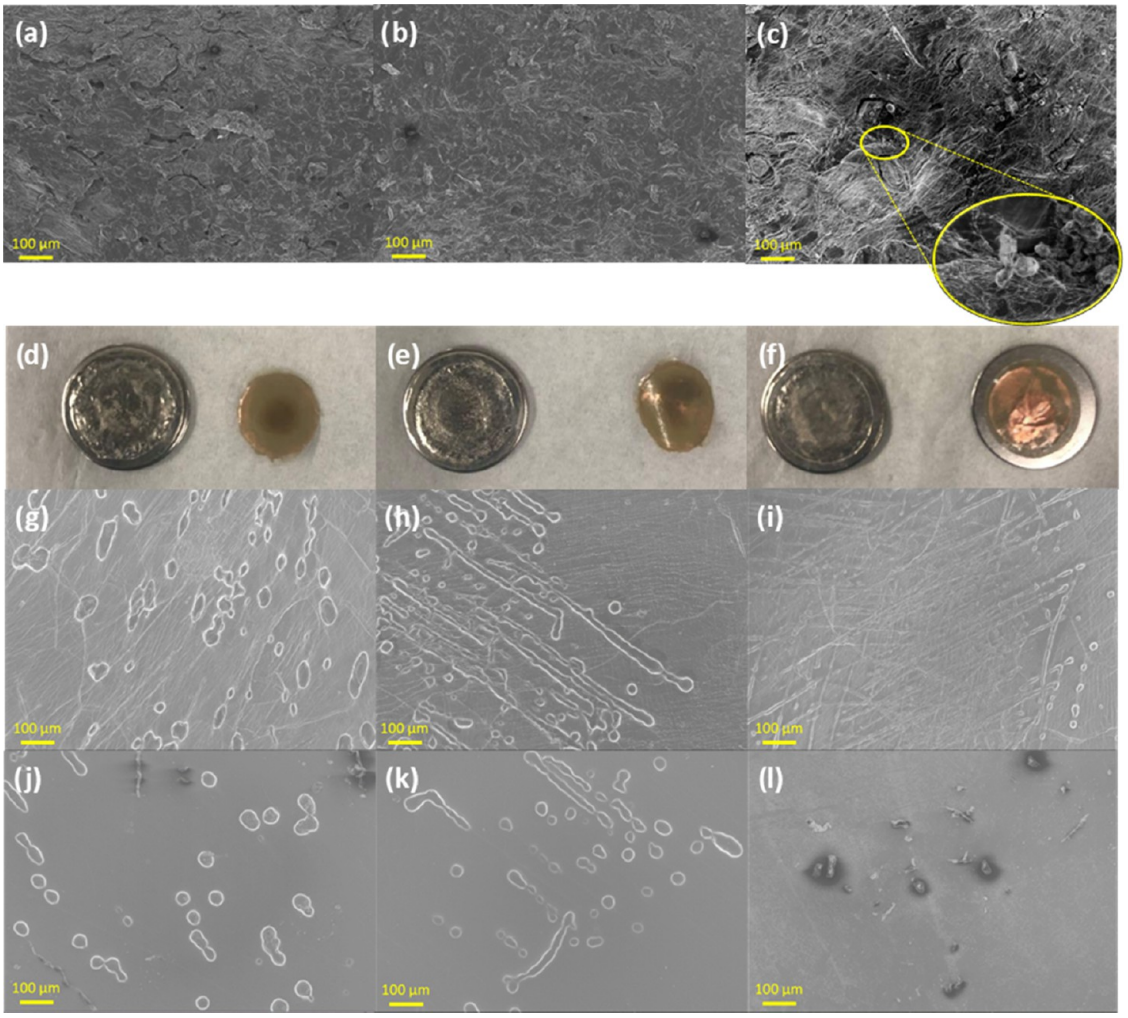

Figure 6. (a–c) SEM images of lithium surfaces after long-term cycling performance (500 cycles at 1C) of NMC622||Li cells at 60 °C with electrolytes of (1), (3), and (4). Images of (d–f) dissembled Cu||Li cells and (g–l) SEM images after single-side plating with the electrolytes of (1), (3), and (4), respectively. Top view (g–i) of stripped lithium surfaces and (j–l) polymer membranes covering on the plated Cu substrate.

Morphologies of Deposited Lithium and Stability of SEI. To evaluate the morphology of ill-defined localized lithium deposits reflecting any inhomogeneity of electrolyte membranes, SEM is a straightforward tool. The images display that lithium surfaces of cells operated with electrolytes (1) and (3) exhibit comparable morphologies of two-dimensional (2D)-planar lithium deposits after long-term cycling in full cells at 60 °C (Figure 6a,b), while the lithium surface of cells cycled with electrolyte (4) rather have more localized nuclei of lithium deposits, even exhibiting dendritic shapes (Figure 6c), essentially corroborating the fact that cell failure in the case of electrolyte (4) is solely due to inhomogeneous lithium deposition.

In view of the careful validation that instability of SEI layers is also not likely the major factor causing cell failure in the case of electrolyte (4), Cu||Li cells with corresponding electrolytes were employed to monitor irreversible electrochemical reactions during cycling.[68] As illustrated in Figure 7a–c, cells with electrolyte (4) rapidly experience unanticipated short circuit within 44 cycles, whereas cells with electrolyte (1) and electrolyte (3) show rather stable performance over 200 cycles. Since the average values of Coulombic efficiency (CE) prior to cell failure (before the 44th cycle) are similar among the three considered electrolyte materials [(1): 83%, (3): 83.7%, and (4): 83.3%], it may be concluded that the morphologies and distribution of deposited lithium instead of instability of SEI and "dead lithium" formations determine cell longevity in this system.[47]

Single-side lithium plating onto Cu at a higher current density (0.2 mA cm^{-2}) was executed at 20 °C for 10 h to obtain a clearer difference of deposited lithium morphologies between samples. As displayed in Figure 7d, cell operation with electrolyte (4) in the worst case was terminated after merely 2 h of plating (0.08 mg of deposited lithium on Cu) due to a short circuit, while electrolytes (1) and (3) allowed operation for periods of >10 h (0.41 mg of deposited lithium on Cu). Additional data of single-side plating of electrolytes (2) and (3) in Li||Li cells is provided in Figure S9 (Supporting Information). Afterward, Cu||Li cells were carefully dissembled for SEM inspection. In Figure 6d–f, it is noticed that the distribution of deposited lithium onto Cu in cells operated with electrolyte (4) appears rather concentrated in certain areas, and most other areas of the electrode surface remain "clean", yet the lithium deposits are evenly spread in the case of the other two electrolytes. For electrolyte (4), the corresponding SEM images (Figure 6g–i) display that cavities of the lithium-stripped surface are not so pronounced when compared to the other electrolytes due to short circuit. As

https://doi.org/10.1021/acsaem.3c00571
ACS Appl. Energy Mater. 2023, 6, 4422–4436

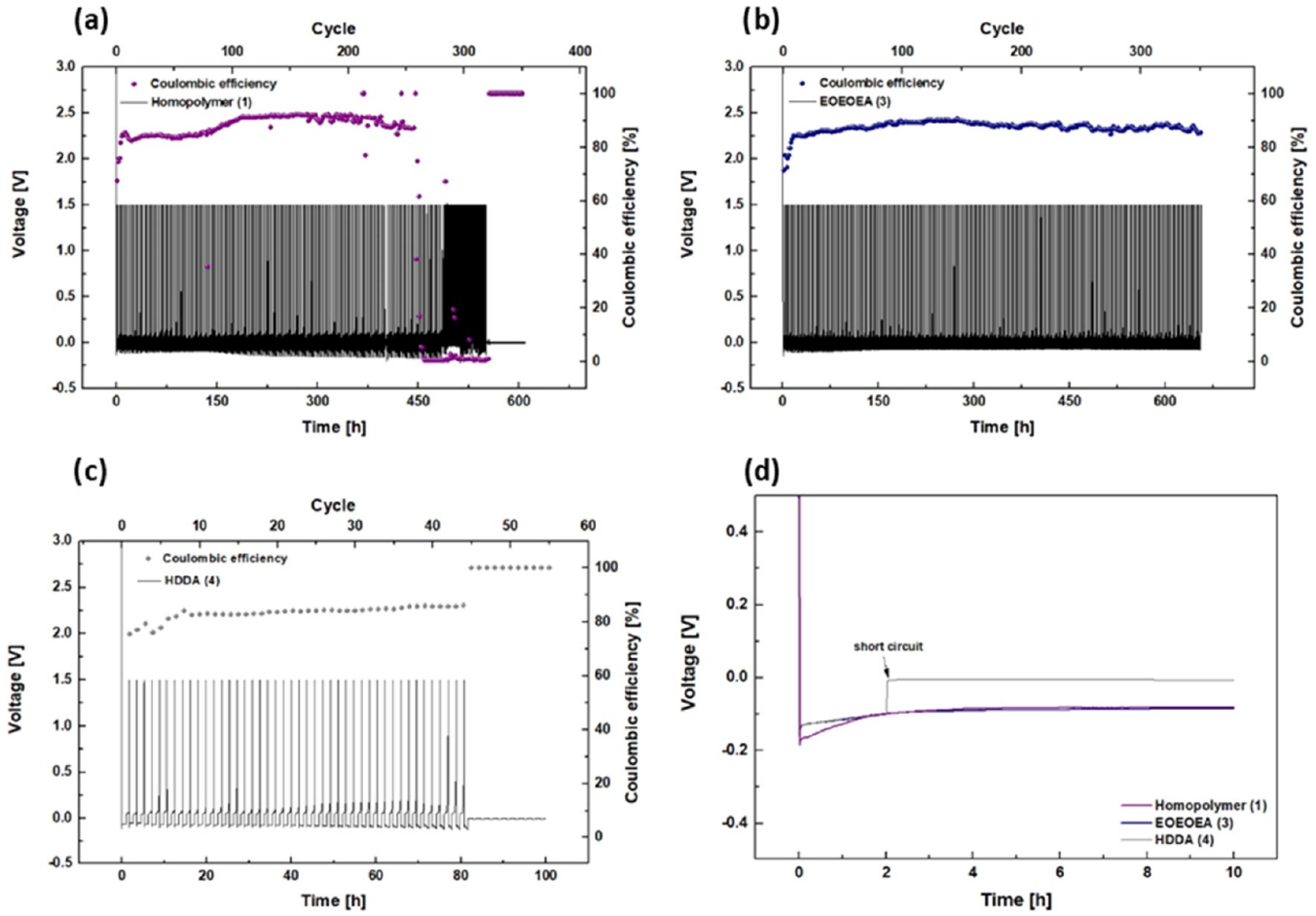

Figure 7. Results of Cu||Li cells with electrolytes of (a) (1), (b) (3), and (c) (4) cycling at 0.1 mA cm^{-2} (1 h per half-cycle, cutoff voltage at 1.5 V) and 20 °C. (d) Result of single-side plating for 10 h at 0.2 mA cm^{-2} (0.41 mg of deposited lithium on Cu) and 20 °C.

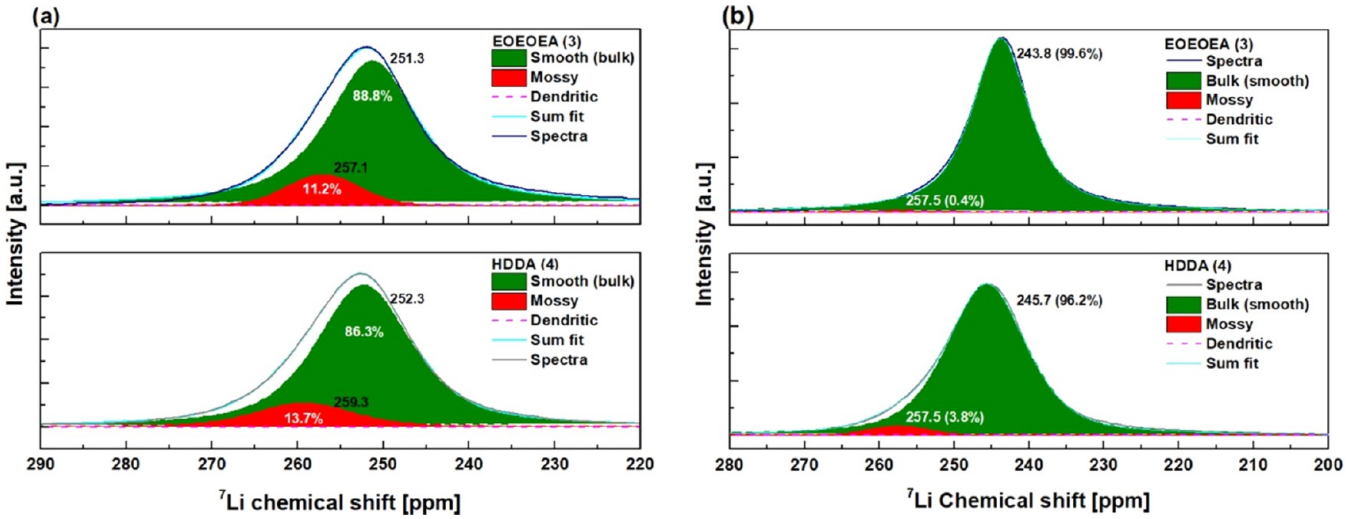

Figure 8. ^{7}Li solid-state NMR spectra (with deconvolution) of (a) lithium-plated (~0.16 mg) Cu substrates with electrolytes of (3) and (4) after the operation of single-side plating in Cu||Li coin cells and (b) NMC||Li cells measured at the 41st charging state after 40 cycles at 0.2C and 20 °C.

illustrated in Figure 6j–l, distinguishable differences can be readily observed for lithium deposit morphologies under each polymer membrane, especially in the case of electrolyte (4), where small fractions of localized and dendritic lithium piercing the membrane are identified (an overview of the membrane shown in Figure S10, Supporting Information), suggesting that the cell failures originate from membrane inhomogeneity.

Besides SEM data, ^{7}Li solid-state NMR enables monitoring of lithium deposit morphologies based on characteristic chemical shifts of the individual lithium microstructures ["dendritic" (~270 μm), "mossy" (~260 μm), or "smooth"

https://doi.org/10.1021/acsaem.3c00571
ACS Appl. Energy Mater. 2023, 6, 4422–4436

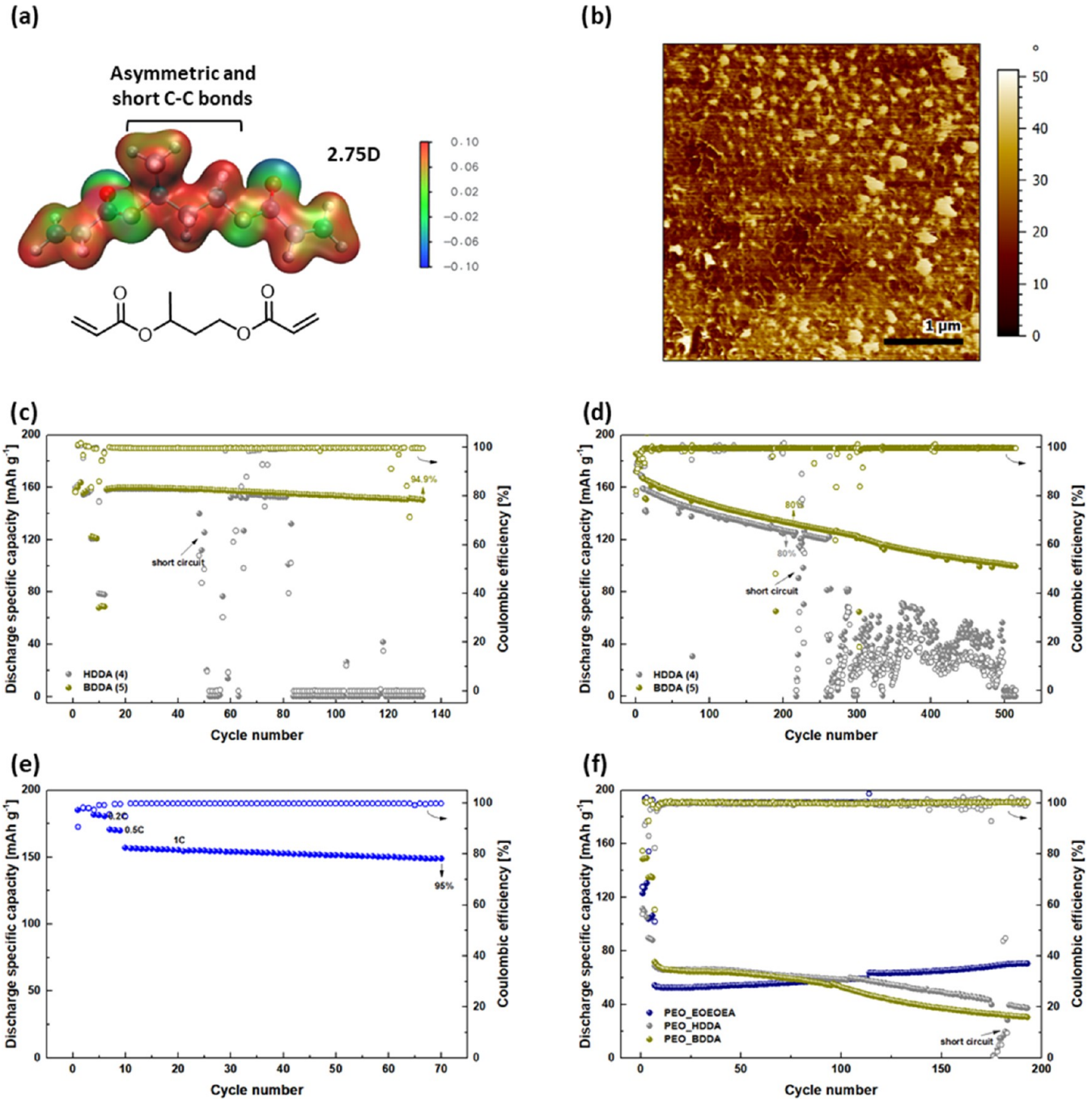

Figure 9. (a) Calculated electrostatic potential around each atom on the segment of the secondary species BDDA (dipole moment: 2.75D in Boltzmann average); the color blue indicates negative potential corresponding to attraction of the proton, while the color red refers to positive potential corresponding to repulsion of the proton. (b) AFM phase image of electrolyte (5). Cycling performance of NMC622||Li cells was conducted at (c) 20 °C and (d) 60 °C with electrolyte (5) in comparison with electrolyte (4). At 20 °C, a formation step including 0.1/0.2/0.5/1C (3 cycles for each rate) was applied, and the long-term cycling proceeded at 0.2C for 120 cycles; at 60 °C, a formation step of 0.1/0.2/0.5/1/2C (3 cycles for each rate) and 1C was applied for long-term performance. (e) Cycling performance in the thick NMC622 (filtrated with electrolyte (3)) ||Li cell with the optimized electrolyte (3) at 1C and 60 °C. (f) Cycling performance in NMC622||Li with PEO-based electrolytes at 0.2C and 20 °C; formation step: 0.05/0.1C (3 cycles at each rate).

(~245 μm)].[47,69] After single-side lithium plating onto Cu at a current density of 0.2 mA cm^{-2}, Cu||Li cells were disassembled, and Cu substrates were subjected to ^{7}Li NMR measurements (Figure 8a). The result highlights that although the lithium deposits mostly exhibit smooth and mossy microstructures in the case of both polymer electrolytes, the ^{7}Li NMR signals in the case of electrolyte (4) appear broader, and the peak extends toward higher chemical shifts. Slightly higher fractions of mossy deposits (13.7%) also indicate that the detected lithium metal deposits are comparatively rough at their surface.

In another experiment of NMC622||Li cells running for 40 cycles (Figure 8b), a similar trend was recognized, showing a wider range of lithium signals and a higher fraction of mossy deposits (3.8%) in electrolyte (4). Nevertheless, the differences of the corresponding ^{7}Li NMR shifts of the metallic lithium species are not particularly pronounced between the analyzed

https://doi.org/10.1021/acsaem.3c00571
ACS Appl. Energy Mater. 2023, 6, 4422−4436

polymer materials despite cell instabilities being readily noticeable in the case of electrolyte (4) (e.g., voltage noise displayed in Figure S11, Supporting Information), which might be caused by lesser amounts of lithium derived from the thin cathode participating in electrochemical cycling. Overall, it is demonstrated that the compatibility between polymer segments not only influences the electrolyte property distributions associated with the consistency of the ion transport rate but also determines the homogeneity of lithium deposition and thus the cycling stability.

Improved Cell Performance due to the Decrement of Nonpolar Bonds of Polymer Segments. Considering the enhancement of similarity of electrostatic fields between copolymer segments that enables to afford homogeneity of the relevant membrane properties, a slight modification of the series of nonpolar carbon bonds of the monomer HDDA may assist in boosting the observable cycling performance. This verification was carried out based on a bifunctional monomer of BDDA as the secondary segment species possessing similar C−C covalent bonds as HDDA but with a shorter and asymmetric structure that offers more differences between the electrostatic potentials of neighboring atoms while decreasing the number of nonpolar bonds and thereby increasing overall molecular polarity (see Figure 9a).[70] The achieved mechanical strength and lithium-ion conductivity of electrolyte (5) are close to the characteristics of electrolyte (4) (see the comparisons in Figure S12, Supporting Information) due to analogous cross-linking densities and similar types of covalent bonds. In view of the improved compatibility between the employed polymer segment species, the degree of phase separation should be mitigated within electrolyte (5), as shown in Figure 9b, illustrating the absence of clear phase boundaries (topography image in Figure S4c).

The corresponding cell-cycling stability is indeed ameliorated when operating electrolyte (5), clearly emphasizing the impact of better membrane homogeneity, while exhibiting the absence of cell short circuits over 100 cycles at both operational temperatures of 20 and 60 °C and similar trends of capacity retention compared to electrolyte (4) (Figure 9c,d). Moreover, with the optimized electrolyte (3) in this PTMC-based system, full cycling performance against a thicker cathode (mass loading: 6.3 mg cm^{-2}) is also feasible at 1C and 60 °C, showing quite promising capacity retention (Figure 9e). To confirm the fact that the proposed concept is also functioning well in other polymer systems, commonly used oligomers of poly(ethylene glycol)diacrylate (PEGDA) in the literature (Figure 1) were employed to replace PTMC-GCDs as the primary polymer species.[17,18,20,21,23,28] In Figure 9f, the electrochemical performance of NMC622||Li cells operated with electrolyte PEO_EOEOEA gradually enhances, likely indicating the formation of more effective and robust interphases upon cycling. Likewise, interphase formation in this case may need more time (≫12 h) for actually achieving equilibrium or metastable conditions. But overall, all cells with the PEO-based electrolytes provide very limited capacity (around 65 mAh g^{-1}), meaning only a small amount of lithium can really participate in the stripping and plating process; hence, the possibility of forming lithium protrusions that cause cycling termination requires more cycles (e.g., after 175 cycles, the first case of short circuit occurred in PEO_HDDA). Also, data of lithium single-side plating shown in Figure S13 (Supporting Information) reveal unstable electrochemical behavior after 62 h in the cells operated with the PEO-based electrolyte containing HDDA segments and ameliorated performance in the cells operated with other electrolytes possessing more compatible copolymer segments. In summary, this experimental approach successfully demonstrates that the homogeneity of electrolyte properties affects relevant electrochemical features including cycling performance, e.g., due to nonuniformity of charge carrier transport, thereby introducing an important parameter and strategy toward the targeted design of advanced copolymer electrolytes. Note that in a future work, a reduction of the cell operation temperatures might be achieved upon combination of segment-tailored polymers with recently introduced thermally responsive electrolytes,[71,72] creating synergies based on robust and homogeneous SEI formation as well as enhanced thermal stability, thereby potentially bestowing the ability to delay the thermal runaway of the cycled cells, also enabling cell operation at ambient temperatures.

CONCLUSIONS

The development of novel polymer electrolytes can involve a tedious series of trial and error attempts that consume time and energy, thus necessitating comprehensive guidelines for tailored electrolyte design. As part of a rational approach to quasi-solid copolymer electrolytes, the impact of structural chemistry of copolymer segments on the reversibility and morphology of lithium metal deposition is elucidated. Indeed, careful selection of reactive monomer and/or oligomer species possessing similar electrostatic fields or polarity in their structures enables one to effectively enhance the resulting homogeneity of copolymer electrolyte membranes suitable for operation in lithium metal batteries, in this way controlling the consistency of charge carrier transport and avoiding growth of severely localized lithium protrusions. This notion is not only indicated from the trend of cell longevities in a number of studies but also validated in a unique PTMC-based system and generally in PEO-based electrolytes. Overall, the introduced concept facilitates guidance for the more systematic tailoring and modeling of structures for future copolymer electrolytes.

ASSOCIATED CONTENT

Supporting Information

The Supporting Information is available free of charge at https://pubs.acs.org/doi/10.1021/acsaem.3c00571.

^{1}H NMR/GPC data of PTMC-grafted cyclodextrins, schematic representation of network structures, details of DFT and molecular dynamics simulation, partial charges of constituents and polymers, structural and RDF data, AFM topography and SEM images, DSC traces and solubility data, Nyquist plots and impedance data from equivalent circuit fitting, and conductivities and additional electrochemical data (Li plating, galvanostatic data) (PDF)

AUTHOR INFORMATION

Corresponding Author

Gunther Brunklaus − *Forschungszentrum Jülich GmbH, Helmholtz-Institute Münster, Münster 48149, Germany;* orcid.org/0000-0003-0030-1383; Email: g.brunklaus@fz-juelich.de

https://doi.org/10.1021/acsaem.3c00571
ACS Appl. Energy Mater. 2023, 6, 4422−4436

Authors

Min-Huei Chiou − *Forschungszentrum Jülich GmbH, Helmholtz-Institute Münster, Münster 48149, Germany;* orcid.org/0000-0002-3259-4857

Elisabeth Verweyen − *Forschungszentrum Jülich GmbH, Helmholtz-Institute Münster, Münster 48149, Germany*

Diddo Diddens − *Forschungszentrum Jülich GmbH, Helmholtz-Institute Münster, Münster 48149, Germany;* orcid.org/0000-0002-2137-1332

Lennart Wichmann − *Forschungszentrum Jülich GmbH, Helmholtz-Institute Münster, Münster 48149, Germany*

Christina Schmidt − *Forschungszentrum Jülich GmbH, Helmholtz-Institute Münster, Münster 48149, Germany*

Kerstin Neuhaus − *Forschungszentrum Jülich GmbH, Helmholtz-Institute Münster, Münster 48149, Germany*

Aditya Choudhary − *Department of Materials Science and Engineering, University of Utah, Salt Lake City, Utah 84112, United States*

Dmitry Bedrov − *Department of Materials Science and Engineering, University of Utah, Salt Lake City, Utah 84112, United States;* orcid.org/0000-0002-3884-3308

Martin Winter − *Forschungszentrum Jülich GmbH, Helmholtz-Institute Münster, Münster 48149, Germany; MEET Battery Research Center, University of Münster, Münster 48149, Germany*

Complete contact information is available at: https://pubs.acs.org/10.1021/acsaem.3c00571

Notes

The authors declare no competing financial interest.

■ ACKNOWLEDGMENTS

The authors M.-H.C., M.W., and G.B. gratefully acknowledge the generous support by the German Federal Ministry of Education and Research (BMBF) within "FB2-POLY" (13XP0429A) and "LiSI" (13XP0224A). Special thanks to Susanna Krämer for measuring DSC data, Dr. Yi-Chen Hsieh for SEM operation, and Dr. Kristina Borzutzki as well as Marvin Mohrhardt for fruitful discussions.

■ REFERENCES

(1) Yao, P.; Yu, H.; Ding, Z.; Liu, Y.; Lu, J.; Lavorgna, M.; Wu, J.; Liu, X. Review on Polymer-Based Composite Electrolytes for Lithium Batteries. *Front. Chem.* **2019**, *7*, No. 522.

(2) Zhang, N.; Du, L.; Zhang, J.; Xu, H.; Zhou, X.; Mai, L.; Xu, L. Self-Assembled Tent-Like Nanocavities for Space-Confined Stable Lithium Metal Anode. *Adv. Funct. Mater.* **2023**, No. 2210862.

(3) Li, Q.; Pan, H.; Li, W.; Wang, Y.; Wang, J.; Zheng, J.; Yu, X.; Li, H.; Chen, L. Homogeneous Interface Conductivity for Lithium Dendrite-Free Anode. *ACS Energy Lett.* **2018**, *3*, 2259.

(4) Xu, H.; Sun, C.; Zhang, S.; Zhang, H.; Liu, Z.; Tang, Y.; Cui, G. A Rigid-Tough Coupling Strategy Engineering Mechanochemically Stable SEI towards Long-Life Lithium Metal Batteries. *ChemSusChem* **2023**, No. e202202334.

(5) Chazalviel, J. N. Electrochemical aspects of the generation of ramified metallic electrodeposits. *Phys. Rev. A* **1990**, *42*, 7355.

(6) Monroe, C.; Newman, J. The Impact of Elastic Deformation on Deposition Kinetics at Lithium/Polymer Interfaces. *J. Electrochem. Soc.* **2005**, *152*, A396.

(7) Khurana, R.; Schaefer, J. L.; Archer, L. A.; Coates, G. W. Suppression of Lithium Dendrite Growth Using Cross-Linked Polyethylene/Poly(ethylene oxide) Electrolytes: A New Approach for Practical Lithium-Metal Polymer Batteries. *J. Am. Chem. Soc.* **2014**, *136*, 7395.

(8) Lu, Q.; Fang, J.; Yang, J.; Miao, R.; Wang, J.; Nuli, Y. Novel cross-linked copolymer gel electrolyte supported by hydrophilic polytetrafluoroethylene for rechargeable lithium batteries. *J. Membr. Sci.* **2014**, *449*, 176.

(9) Long, L.; Wang, S.; Xiao, M.; Meng, Y. Polymer electrolytes for lithium polymer batteries. *J. Mater. Chem. A* **2016**, *4*, 10038.

(10) Young, W.-S.; Kuan, W.-F.; Epps, I.; Thomas, H. Block copolymer electrolytes for rechargeable lithium batteries. *J. Polym. Sci., Part B: Polym. Phys.* **2014**, *52*, 1.

(11) Kambe, Y.; Arges, C. G.; Czaplewski, D. A.; Dolejsi, M.; Krishnan, S.; Stoykovich, M. P.; de Pablo, J. J.; Nealey, P. F. Role of Defects in Ion Transport in Block Copolymer Electrolytes. *Nano Lett.* **2019**, *19*, 4684.

(12) Sharon, D.; Bennington, P.; Dolejsi, M.; Webb, M. A.; Dong, B. X.; de Pablo, J. J.; Nealey, P. F.; Patel, S. N. Intrinsic Ion Transport Properties of Block Copolymer Electrolytes. *ACS Nano* **2020**, *14*, 8902.

(13) Wang, G.; Li, J.; Shang, L.; He, H.; Cui, T.; Chai, S.; Zhao, C.; Wu, L.; Li, H. Nanostructured Polymer Composite Electrolytes with Self-Assembled Polyoxometalate Networks for Proton Conduction. *CCS Chem.* **2021**, *4*, 151.

(14) Borzutzki, K.; Dong, K.; Nair, J. R.; Wolff, B.; Hausen, F.; Eichel, R.-A.; Winter, M.; Manke, I.; Brunklaus, G. Lithium deposition in single-ion conducting polymer electrolytes. *Cell Rep. Phys. Sci.* **2021**, *2*, No. 100496.

(15) Zhang, J.; Farias-Mancilla, B.; Destarac, M.; Schubert, U. S.; Keddie, D. J.; Guerrero-Sanchez, C.; Harrisson, S. Asymmetric Copolymers: Synthesis, Properties, and Applications of Gradient and Other Partially Segregated Copolymers. *Macromol. Rapid Commun.* **2018**, *39*, No. 1800357.

(16) Ramos-Garcés, M. V.; Li, K.; Lei, Q.; Bhattacharya, D.; Kole, S.; Zhang, Q.; Strzalka, J.; Angelopoulou, P. P.; Sakellariou, G.; Kumar, R.; Arges, C. G. Understanding the ionic activity and conductivity value differences between random copolymer electrolytes and block copolymer electrolytes of the same chemistry. *RSC Adv.* **2021**, *11*, 15078.

(17) Song, M.-K.; Cho, J.-Y.; Cho, B. W.; Rhee, H.-W. Characterization of UV-cured gel polymer electrolytes for rechargeable lithium batteries. *J. Power Sources* **2002**, *110*, 209.

(18) Cheng, C. L.; Wan, C. C.; Wang, Y. Y. Preparation of porous, chemically cross-linked, PVdF-based gel polymer electrolytes for rechargeable lithium batteries. *J. Power Sources* **2004**, *134*, 202.

(19) Choi, N.-S.; Park, J.-K. A comparative study of coordination between host polymers and Li+ ions in UV-cured gel polymer electrolytes. *Solid State Ionics* **2009**, *180*, 1204.

(20) Shi, J.; Hu, H.; Xia, Y.; Liu, Y.; Liu, Z. Polyimide matrix-enhanced cross-linked gel separator with three-dimensional heat-resistance skeleton for high-safety and high-power lithium ion batteries. *J. Mater. Chem. A* **2014**, *2*, 9134.

(21) Lu, Q.; Yang, J.; Lu, W.; Wang, J.; Nuli, Y. Advanced semi-interpenetrating polymer network gel electrolyte for rechargeable lithium batteries. *Electrochim. Acta* **2015**, *152*, 489.

(22) Chaudoy, V.; Ghamouss, F.; Luais, E.; Tran-Van, F. Cross-Linked Polymer Electrolytes for Li-Based Batteries: From Solid to Gel Electrolytes. *Ind. Eng. Chem. Res.* **2016**, *55*, 9925.

(23) Fan, W.; Li, N.-W.; Zhang, X.; Zhao, S.; Cao, R.; Yin, Y.; Xing, Y.; Wang, J.; Guo, Y.-G.; Li, C. A Dual-Salt Gel Polymer Electrolyte with 3D Cross-Linked Polymer Network for Dendrite-Free Lithium Metal Batteries. *Adv. Sci.* **2018**, *5*, No. 1800559.

(24) Baik, J.-H.; Kim, S.; Hong, D. G.; Lee, J.-C. Gel Polymer Electrolytes Based on Polymerizable Lithium Salt and Poly(ethylene glycol) for Lithium Battery Applications. *ACS Appl. Mater. Interfaces* **2019**, *11*, 29718.

(25) Dai, K.; Ma, C.; Feng, Y.; Zhou, L.; Kuang, G.; Zhang, Y.; Lai, Y.; Cui, X.; Wei, W. A borate-rich, cross-linked gel polymer electrolyte with near-single ion conduction for lithium metal batteries. *J. Mater. Chem. A* **2019**, *7*, 18547.

(26) Xiao, Q.; Deng, C.; Wang, Q.; Zhang, Q.; Yue, Y.; Ren, S. In Situ Cross-Linked Gel Polymer Electrolyte Membranes with Excellent Thermal Stability for Lithium Ion Batteries. *ACS Omega* **2019**, *4*, 95.
(27) Ahmed, F.; Kim, D.; Lei, J.; Ryu, T.; Yoon, S.; Zhang, W.; Lim, H.; Jang, G.; Jang, H.; Kim, W. UV-Cured Cross-Linked Astounding Conductive Polymer Electrolyte for Safe and High-Performance Li-Ion Batteries. *ACS Appl. Mater. Interfaces* **2021**, *13*, 34102.
(28) Long, M.-C.; Wang, T.; Duan, P.-H.; Gao, Y.; Wang, X.-L.; Wu, G.; Wang, Y.-Z. Thermotolerant and fireproof gel polymer electrolyte toward high-performance and safe lithium-ion battery. *J. Energy Chem.* **2022**, *65*, 9.
(29) Wang, Q.; Zhang, P.; Zhu, W.; Zhang, D.; Li, Z.; Wang, H.; Sun, H.; Wang, B.; Fan, L.-Z. A two-step strategy for constructing stable gel polymer electrolyte interfaces for long-life cycle lithium metal batteries. *J. Materiomics* **2022**, *8*, 1048.
(30) Chiou, M.-H.; Borzutzki, K.; Thienenkamp, J. H.; Mohrhardt, M.; Liu, K.-L.; Mereacre, V.; Binder, J. R.; Ehrenberg, H.; Winter, M.; Brunklaus, G. Durable fast-charging lithium metal batteries designed with cross-linked polymer electrolytes and niobate-coated cathode. *J. Power Sources* **2022**, *538*, No. 231528.
(31) Frisch, M. J.; Trucks, G. W.; Schlegel, H. B.; Scuseria, G. E.; Robb, M. A.; Cheeseman, J. R.; Scalmani, G.; Barone, V.; Petersson, G. A.; Nakatsuji, H.; Li, X.; Caricato, M.; Marenich, A. V.; Bloino, J.; Janesko, B. G.; Gomperts, R.; Mennucci, B.; Hratchian, H. P.; Ortiz, J. V.; Izmaylov, A. F.; Sonnenberg, J. L.; Williams; Ding, F.; Lipparini, F.; Egidi, F.; Goings, J.; Peng, B.; Petrone, A.; Henderson, T.; Ranasinghe, D.; Zakrzewski, V. G.; Gao, J.; Rega, N.; Zheng, G.; Liang, W.; Hada, M.; Ehara, M.; Toyota, K.; Fukuda, R.; Hasegawa, J.; Ishida, M.; Nakajima, T.; Honda, Y.; Kitao, O.; Nakai, H.; Vreven, T.; Throssell, K.; Montgomery, J. A., Jr.; Peralta, J. E.; Ogliaro, F.; Bearpark, M. J.; Heyd, J. J.; Brothers, E. N.; Kudin, K. N.; Staroverov, V. N.; Keith, T. A.; Kobayashi, R.; Normand, J.; Raghavachari, K.; Rendell, A. P.; Burant, J. C.; Iyengar, S. S.; Tomasi, J.; Cossi, M.; Millam, J. M.; Klene, M.; Adamo, C.; Cammi, R.; Ochterski, J. W.; Martin, R. L.; Morokuma, K.; Farkas, O.; Foresman, J. B.; Fox, D. J. *Gaussian 16*, revision C.01; Gaussian Inc.: Wallingford, CT, 2016.
(32) Marenich, A. V.; Cramer, C. J.; Truhlar, D. G. Universal Solvation Model Based on Solute Electron Density and on a Continuum Model of the Solvent Defined by the Bulk Dielectric Constant and Atomic Surface Tensions. *J. Phys. Chem. B* **2009**, *113*, 6378.
(33) Borodin, O.; Behl, W.; Jow, T. R. Oxidative Stability and Initial Decomposition Reactions of Carbonate, Sulfone, and Alkyl Phosphate-Based Electrolytes. *J. Phys. Chem. C* **2013**, *117*, 8661.
(34) Borodin, O.; Olguin, M.; Spear, C. E.; Leiter, K. W.; Knap, J. Towards high throughput screening of electrochemical stability of battery electrolytes. *Nanotechnology* **2015**, *26*, No. 354003.
(35) Hall, D. S.; Self, J.; Dahn, J. R. Dielectric Constants for Quantum Chemistry and Li-Ion Batteries: Solvent Blends of Ethylene Carbonate and Ethyl Methyl Carbonate. *J. Phys. Chem. C* **2015**, *119*, 22322.
(36) Melitz, W.; Shen, J.; Kummel, A. C.; Lee, S. Kelvin probe force microscopy and its application. *Surf. Sci. Rep.* **2011**, *66*, 1.
(37) Borodin, O. Polarizable Force Field Development and Molecular Dynamics Simulations of Ionic Liquids. *J. Phys. Chem. B* **2009**, *113*, 11463.
(38) Bedrov, D.; Piquemal, J.-P.; Borodin, O.; MacKerell, A. D., Jr.; Roux, B.; Schröder, C. Molecular Dynamics Simulations of Ionic Liquids and Electrolytes Using Polarizable Force Fields. *Chem. Rev.* **2019**, *119*, 7940.
(39) Choudhary, A.; Dong, D.; Bedrov, D. Li+ Transport in Ethylene Carbonate Based Comb-Branched Solid Polymer Electrolyte: A Molecular Dynamics Simulation Study. *ACS Appl. Polym. Mater.* **2022**, *4*, 8496.
(40) Dong, D.; Choudhary, A.; Bedrov, D. Coupling−Decoupling Transition between Li+ Transport and Segmental Relaxation in Solid Polymer Electrolytes. *ACS Appl. Polym. Mater.* **2020**, *2*, 5358.
(41) Chen, Y.-H.; Hsieh, Y.-C.; Liu, K. L.; Wichmann, L.; Thienenkamp, J. H.; Choudhary, A.; Bedrov, D.; Winter, M.; Brunklaus, G. Green Polymer Electrolytes Based on Polycaprolactones for Solid-State High-Voltage Lithium Metal Batteries. *Macromol. Rapid Commun.* **2022**, *43*, No. 2200335.
(42) Thole, B. T. Molecular polarizabilities calculated with a modified dipole interaction. *Chem. Phys.* **1981**, *59*, 341.
(43) Palmer, B. J. Direct Application of Shake to the Velocity Verlet Algorithm. *J. Comput. Phys.* **1993**, *104*, 470.
(44) Hoover, W. G. Canonical dynamics: Equilibrium phase-space distributions. *Phys. Rev. A* **1985**, *31*, 1695.
(45) Evans, D. J.; Holian, B. L. The Nose−Hoover thermostat. *J. Chem. Phys.* **1985**, *83*, 4069.
(46) Martyna, G. J.; Tuckerman, M. E.; Tobias, D. J.; Klein, M. L. Explicit reversible integrators for extended systems dynamics. *Mol. Phys.* **1996**, *87*, 1117.
(47) Hsieh, Y.-C.; Leißing, M.; Nowak, S.; Hwang, B.-J.; Winter, M.; Brunklaus, G. Quantification of Dead Lithium via In Situ Nuclear Magnetic Resonance Spectroscopy. *Cell Rep. Phys. Sci.* **2020**, *1*, No. 100139.
(48) Nishimoto, A.; Watanabe, M.; Ikeda, Y.; Kohjiya, S. High ionic conductivity of new polymer electrolytes based on high molecular weight polyether comb polymers. *Electrochim. Acta* **1998**, *43*, 1177.
(49) Dvir, H.; Jopp, J.; Gottlieb, M. Estimation of polymer−surface interfacial interaction strength by a contact AFM technique. *J. Colloid Interface Sci.* **2006**, *304*, 58.
(50) Li, L.; Chan, C.-M.; Yeung, K. L.; Li, J.-X.; Ng, K.-M.; Lei, Y. Direct Observation of Growth of Lamellae and Spherulites of a Semicrystalline Polymer by AFM. *Macromolecules* **2001**, *34*, 316.
(51) de Graaf, L.; Möller, M. Glass transition temperatures of microphase-separated semi-interpenetrating polymer networks of polystyrene-inter-poly(cross-2-ethylhexyl methacrylate). *Polymer* **1995**, *36*, 3451.
(52) Tanaka, K.; Takahara, A.; Kajiyama, T. Surface molecular motion in thin films of poly(styrene-block-methyl methacrylate) diblock copolymer. *Acta Polym.* **1995**, *46*, 476.
(53) Jung, R.; Metzger, M.; Maglia, F.; Stinner, C.; Gasteiger, H. A. Oxygen Release and Its Effect on the Cycling Stability of LiNixMnyCozO2(NMC) Cathode Materials for Li-Ion Batteries. *J. Electrochem. Soc.* **2017**, *164*, A1361.
(54) Kim, C. S.; Oh, S. M. Importance of donor number in determining solvating ability of polymers and transport properties in gel-type polymer electrolytes. *Electrochim. Acta* **2000**, *45*, 2101.
(55) Liu, K.; Liu, M.; Cheng, J.; Dong, S.; Wang, C.; Wang, Q.; Zhou, X.; Sun, H.; Chen, X.; Cui, G. Novel cellulose/polyurethane composite gel polymer electrolyte for high performance lithium batteries. *Electrochim. Acta* **2016**, *215*, 261.
(56) Lee, H.; Lim, H.-S.; Ren, X.; Yu, L.; Engelhard, M. H.; Han, K. S.; Lee, J.; Kim, H.-T.; Xiao, J.; Liu, J.; Xu, W.; Zhang, J.-G. Detrimental Effects of Chemical Crossover from the Lithium Anode to Cathode in Rechargeable Lithium Metal Batteries. *ACS Energy Lett.* **2018**, *3*, 2921.
(57) Lee, H.; Lee, D. J.; Kim, Y.-J.; Park, J.-K.; Kim, H.-T. A simple composite protective layer coating that enhances the cycling stability of lithium metal batteries. *J. Power Sources* **2015**, *284*, 103.
(58) Yang, M.; Jue, N.; Chen, Y.; Wang, Y. Improving Cyclability of Lithium Metal Anode via Constructing Atomic Interlamellar Ion Channel for Lithium Sulfur Battery. *Nanoscale Res. Lett.* **2021**, *16*, 52.
(59) Barai, P.; Higa, K.; Srinivasan, V. Lithium dendrite growth mechanisms in polymer electrolytes and prevention strategies. *Phys. Chem. Chem. Phys.* **2017**, *19*, 20493.
(60) Harry, K. J.; Higa, K.; Srinivasan, V.; Balsara, N. P. Influence of Electrolyte Modulus on the Local Current Density at a Dendrite Tip on a Lithium Metal Electrode. *J. Electrochem. Soc.* **2016**, *163*, A2216.
(61) Politzer, P.; Ranganathan, S. Bond-order-bond-energy correlations. *Chem. Phys. Lett.* **1986**, *124*, 527.
(62) Nielsen, L. E. Cross-Linking−Effect on Physical Properties of Polymers. *J. Macromol. Sci., Part C* **1969**, *3*, 69.
(63) Shokuhfar, A.; Arab, B. The effect of cross linking density on the mechanical properties and structure of the epoxy polymers: molecular dynamics simulation. *J. Mol. Model.* **2013**, *19*, 3719.

https://doi.org/10.1021/acsaem.3c00571
ACS Appl. Energy Mater. 2023, 6, 4422−4436

(64) Jeon, O.; Song, S. J.; Lee, K.-J.; Park, M. H.; Lee, S.-H.; Hahn, S. K.; Kim, S.; Kim, B.-S. Mechanical properties and degradation behaviors of hyaluronic acid hydrogels cross-linked at various cross-linking densities. *Carbohydr. Polym.* **2007**, *70*, 251.
(65) Zhang, L.; Rowan, S. J. Effect of Sterics and Degree of Cross-Linking on the Mechanical Properties of Dynamic Poly(alkylurea−urethane) Networks. *Macromolecules* **2017**, *50*, 5051.
(66) Li, C.; Strachan, A. Free volume evolution in the process of epoxy curing and its effect on mechanical properties. *Polymer* **2016**, *97*, 456.
(67) Duan, H.; Yin, Y.-X.; Shi, Y.; Wang, P.-F.; Zhang, X.-D.; Yang, C.-P.; Shi, J.-L.; Wen, R.; Guo, Y.-G.; Wan, L.-J. Dendrite-Free Li-Metal Battery Enabled by a Thin Asymmetric Solid Electrolyte with Engineered Layers. *J. Am. Chem. Soc.* **2018**, *140*, 82.
(68) Xiao, J.; Li, Q.; Bi, Y.; Cai, M.; Dunn, B.; Glossmann, T.; Liu, J.; Osaka, T.; Sugiura, R.; Wu, B.; Yang, J.; Zhang, J.-G.; Whittingham, M. S. Understanding and applying coulombic efficiency in lithium metal batteries. *Nat. Energy* **2020**, *5*, 561.
(69) Hsieh, Y.-C.; Thienenkamp, J. H.; Huang, C.-J.; Tao, H.-C.; Rodehorst, U.; Hwang, B. J.; Winter, M.; Brunklaus, G. Revealing the Impact of Film-Forming Electrolyte Additives on Lithium Metal Batteries via Solid-State NMR/MRI Analysis. *J. Phys. Chem. C* **2021**, *125*, 252.
(70) Furió, C.; Calatayud, M. L. Difficulties with the Geometry and Polarity of Molecules: Beyond Misconceptions. *J. Chem. Educ.* **1996**, *73*, 36.
(71) Jiang, F.-N.; Cheng, X.-B.; Yang, S.-J.; Xie, J.; Yuan, H.; Liu, L.; Huang, J.-Q.; Zhang, Q. Thermoresponsive Electrolytes for Safe Lithium-Metal Batteries. *Adv. Mater.* **2023**, *35*, No. 2209114.
(72) Zhou, Q.; Dong, S.; Lv, Z.; Xu, G.; Huang, L.; Wang, Q.; Cui, Z.; Cui, G. A Temperature-Responsive Electrolyte Endowing Superior Safety Characteristic of Lithium Metal Batteries. *Adv. Energy Mater.* **2020**, *10*, No. 1903441.

https://doi.org/10.1021/acsaem.3c00571
ACS Appl. Energy Mater. 2023, 6, 4422−4436